

A WIDE-FIELD, LOW-FREQUENCY RADIO SURVEY OF THE FIELD OF M31. I. CONSTRUCTION AND STATISTICAL ANALYSIS OF THE SOURCE CATALOG

JOSEPH D. GELFAND

Harvard-Smithsonian Center for Astrophysics, MS-10, 60 Garden Street, Cambridge, MA 02138; jgelfand@cfa.harvard.edu

T. JOSEPH W. LAZIO

Naval Research Laboratory, Code 7213, 4555 Overlook Avenue SW, Washington, DC 20375-5351; joseph.lazio@nrl.navy.mil

AND

B. M. GAENSLER

Harvard-Smithsonian Center for Astrophysics, 60 Garden Street, Cambridge, MA 02138; bgaensler@cfa.harvard.edu

Received 2004 January 24; accepted 2004 April 27

ABSTRACT

We present here the results of a 325 MHz radio survey of M31, conducted with the A configuration of the Very Large Array. The survey covered an area of 7.6 deg^2 , and a total of 405 radio sources between $\leq 6''$ and $170''$ in extent were mapped with a resolution of $6''$ and a 1σ sensitivity of $\sim 0.6 \text{ mJy beam}^{-1}$. For each source, its morphological class, major axis θ_M , minor axis θ_m , position angle θ_{PA} , peak flux I , integrated flux density S , spectral index α , and spectral curvature parameter φ were calculated. A comparison of the flux and radial distribution—both in the plane of the sky and in the plane of M31—of these sources with those of the *XMM-Newton* Large-Scale Structure Survey and Westerbork Northern Sky Survey revealed that a vast majority of sources detected are background radio galaxies. As a result of this analysis, we expect that only a few sources are intrinsic to M31. These sources are identified and discussed in an accompanying paper.

Subject headings: catalogs — galaxies: individual (M31) — radio continuum: galaxies —
 radio continuum: general

Online material: additional figures, machine-readable table

1. INTRODUCTION

In order to understand the dynamics of a galaxy it is crucial to know properties of its radio population. Much has been learned about the Milky Way from radio observations of the supernova remnants (SNRs), H II regions, and pulsars detected within it. However, a complete census of radio sources in the Milky Way is difficult to obtain because of source confusion. In addition, since the distances to these sources are often extremely uncertain, it is difficult to determine their properties. As a result, it is advantageous to observe external galaxies to learn about the dynamics and properties of “normal” galaxies. The first step of this process is to obtain a census of radio populations in a galaxy, and it is for this reason that we have surveyed the radio population of M31, the nearest spiral galaxy.

M31 has been surveyed in the radio before, both as parts of larger surveys such as the Westerbork Northern Sky Survey (WENSS; Rengelink et al. 1997) and NRAO VLA Sky Survey (NVSS; Condon et al. 1998), and as the focus of dedicated surveys such as the 36W (Bystedt et al. 1984), 37W (Walterbos et al. 1985), and Braun (1990) surveys, the properties of all of which are summarized in Table 1. Despite its proximity to the Milky Way, mapping M31 is difficult because its large angular size on the sky ($> 2^\circ$) requires many pointings at higher radio frequencies ($\nu \gtrsim 1 \text{ GHz}$) to fully cover. As a result, existing surveys of M31 are either deep but cover only a small region of M31, or cover the entire optical disk of M31 with relatively poor sensitivity, as shown in Table 1 and Figure 1. Because of this, the radio population of discrete sources in M31 is not well understood. To rectify this situation, we have surveyed M31

with the Very Large Array¹ (VLA) at 325 MHz ($\lambda = 90 \text{ cm}$) using the A configuration, achieving a 1σ sensitivity less than a mJy with a resolution of $6''$ ($\sim 20 \text{ pc}$ at the distance of M31, assumed to be 780 kpc; Stanek & Garnavich 1998) over the entire optical disk of M31 because of the large size of the VLA’s primary beam at this frequency. Using the A configuration has the advantage that extended emission from M31 was resolved out, allowing us to better determine the properties of the compact radio population. As seen in Table 1, the survey presented here does very well in resolution (θ_{res}) versus field of view (FOV) when compared to past surveys of M31 and has a similar sensitivity to that of previous higher frequency surveys.

This paper describes the observations, the data reduction process that led to the final source list, and the statistical properties of the detected sources. This paper is structured as follows: § 2 describes the observations and data reduction techniques used to make the final source list, § 3 presents the final (GLG) source list, § 4 presents the statistical properties of the GLG source list, and § 5 presents the conclusions derived from this analysis. In a companion paper (J. D. Gelfand, T. J. W. Lazio, & B. M. Gaensler 2004, in preparation), we will classify the sources and discuss their properties.

This paper uses the convention of S_ν is the flux density of a source at a frequency ν MHz, radio spectral index α is defined

¹ The VLA is operated by The National Radio Astronomy Observatory, which is a facility of the National Science Foundation operated under cooperative agreement by Associated Universities, Inc.

TABLE 1
SUMMARY OF RADIO SURVEYS

Survey	Observation Date	Frequency (MHz)	Flux Density Limit ^a (mJy)	Resolution (arcsec)	FOV (deg ²)	Number of Sources	Reference
WENSS	1991–1993	325	18	54 × 82	...	288	Rengelink et al. (1997)
36W	1975	610	3	54 × 82	10.1	392	Bystedt et al. (1984)
37W	1975–1979	1412	1	23 × 35	3.1	249	Walterbos et al. (1985)
Braun	1990	1465	0.15	5	1.9	534	Braun (1990)
NVSS	1993–1996	1400	2.5	45	...	831	Condon et al. (1998)
GLG	2000	325	3	6	7.6	405	This paper

^a The flux density limits given for WENSS, 36W, 37W, Braun, and NVSS surveys are the lowest flux densities quoted by these authors. For all surveys but the 36W survey, this corresponds to a 5 σ cutoff. For the 36W survey, this corresponds to a 4 σ cutoff.

as $S_\nu \propto \nu^\alpha$, and the distance to M31 is assumed to be 780 ± 13 kpc (Stanek & Garnavich 1998).

2. OBSERVATIONS AND DATA REDUCTION

This section describes the observations and data reduction process that led to the GLG source list. As detailed below, the data reduction process differs from that of higher frequency observations because of the large field of view. In addition, 325 MHz observations are plagued by radio frequency interference (RFI), which must be removed before imaging.

2.1. Observations

This paper is the result of a 5 hr (~ 4 hr on-source) observation of M31 conducted on 2000 December 15 with the VLA A configuration. The observations were done in spectral line mode with two intermediate frequencies (IFs), centered at 321.6 and 327.5 MHz, each with a bandwidth of 3125 kHz divided into 64 frequency channels. Spectral line mode was used to reduce the effect of primary beam chromatic aberration (bandwidth smearing) and, more importantly, to expedite excision of radio frequency interference (RFI). The receivers recorded both right circular polarization (RCP) and left circular polarization (LCP) data, which means that only Stokes I (total intensity) and Stokes V (circular polarization) were measured. Calibrator sources 3C 405 (Cyg A) and TXS 0035+413 were observed hourly for ~ 5 minutes. Cyg A was used to set the flux density scale and calibrate the bandpass by applying a 333 MHz model to the observed image.² This model assumes that Cyg A has a total flux density of 5983 Jy at 325 MHz, within the 6% error of the Baars flux density scale (Baars et al. 1977). The calibrator source TX 0035+413 was then used to calibrate the visibilities. Table 2 summarizes the properties of the observation.³

2.2. Data Reduction

The initial phase and flux density calibration was done using the AIPS task CALIB. For both Cyg A and TXS 0035+413, edge channels 1–5 and 58–63 were flagged owing to poor frequency response and the visibility data were inspected manually for RFI. During the first half of the first scan of Cyg A, antenna 13 malfunctioned. To preserve data from this antenna

taken in the second half of this scan, all data points involving antenna 13 in the first half of this scan were flagged and the phase and flux solutions calculated for the second half were renormalized. After the flux and phase calibration solutions were calculated, they were applied to all the visibility data, including the M31 visibilities.

The process of converting the raw data into a usable image and source list was a long and complicated one, as illustrated in Figure 2. The major complication in this process is the presence of RFI, and it was necessary to remove as much of it as possible before any imaging. This was accomplished by inspecting each baseline visually for RFI. Both the RCP and LCP data were searched separately for RFI because, being terrestrial in origin, it was often polarized and would appear in one polarization channel but not the other. To avoid complications when calculating the total intensity (Stokes I), flags in one polarization were applied to the other. Since polarized RFI is strong in Stokes V (Stokes $V = \text{RCP} - \text{LCP}$), all baselines were searched for RFI in this Stokes parameter as well.

2.2.1. Image Production

Only after all the RFI was removed was it possible to produce a high-quality image of M31. Owing to its large FOV at 325 MHz, the VLA is not coplanar at this frequency. Therefore, in order to make the image using standard radio techniques, the primary beam was divided into 73 small “facets” over which the VLA can be safely assumed to be coplanar (Cornwell & Perley 1992).

Two sets of images were made, both created by an iterative process of CLEANing and self-calibration. For Images A, the self-calibration process used every positive CLEAN component (CC). As a result, the calibration model included CCs that were peaks in the noise, artificially lowering the noise of the image and increasing the probability of a false detection. However, these maps were good enough to find sources (Source list I) that generated the restrictive clean boxes (CLEAN Boxes 2) used to image Images B.

The second set of images (Images B), which generated the source list presented in this paper, were also created using an iterative process involving the CLEAN algorithm and self-calibration. However, this time CCs were only placed around sources in Source list I and off-axis WENSS sources (CLEAN Boxes 2). The use of smaller clean boxes decreased the possibility of “overcleaning” and removes any CLEAN bias (see Condon et al. 1998 for a good description of CLEAN bias). In addition, the self-calibration process used only the strongest CCs inside the primary beam to maximize the accuracy of the phase calibration model inside the primary beam. Using this

² Available at <http://rsd-www.nrl.navy.mil/7213/lazio/tutorial/VLAmodels/models.html>.

³ The FOV listed in this table is equal to $\text{FOV} = \pi R^2$, where R is the distance in degrees from the pointing center to the most distant source detected. This is larger than the FWHM of the primary beam owing to the shapes of the “facets” discussed in § 2.2.1.

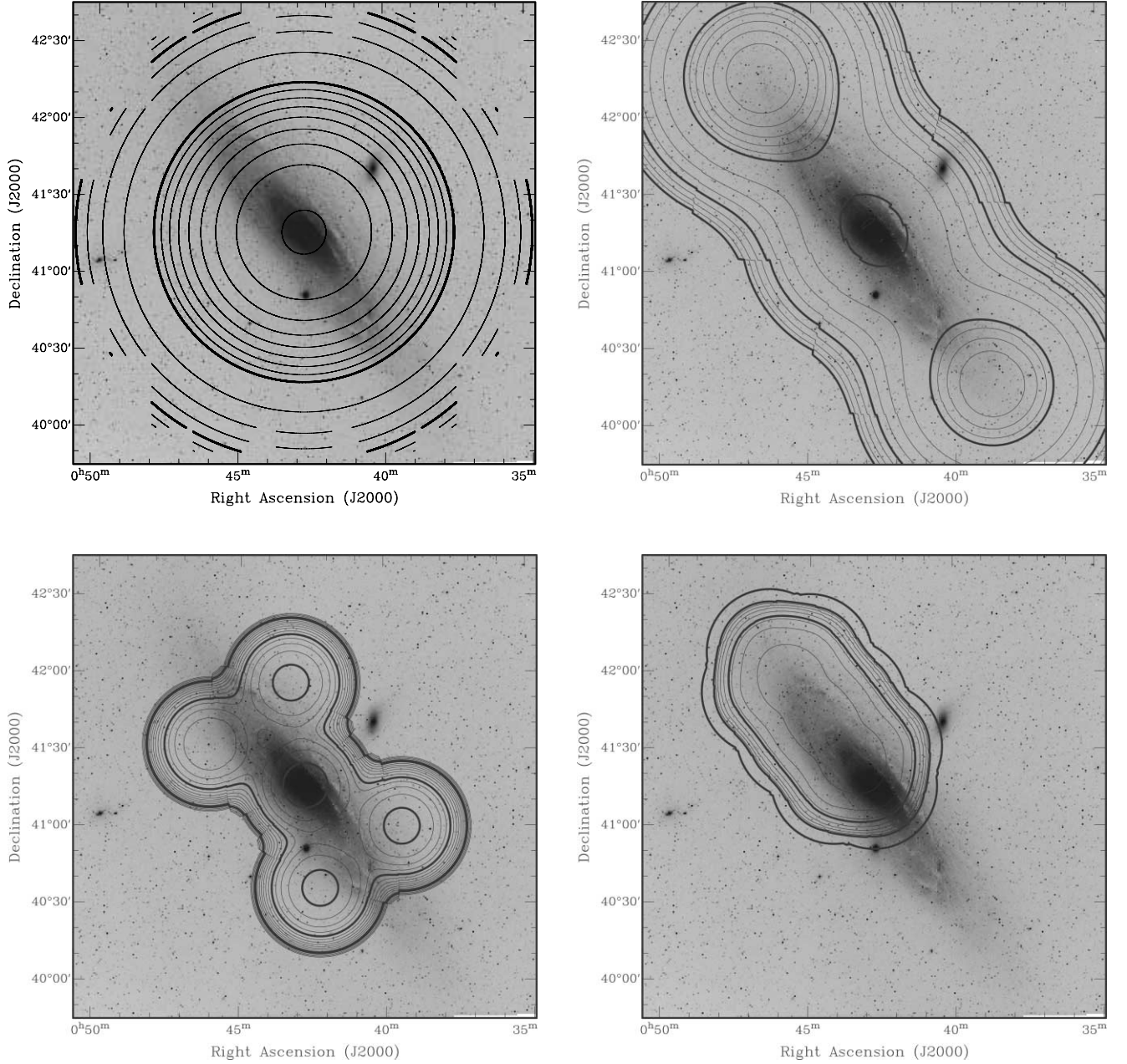


FIG. 1.—Contours showing the 1σ sensitivity of the (clockwise from upper left) GLG (this paper), 36W (Bystedt et al. 1984), Braun (1990), and 37W (Walterbos et al. 1985) radio surveys across the field of M31. The sensitivity for the 36W, Braun, and 37W surveys were generated using the procedure described in § 4.3. The optical image is of M31 from the Palomar Optical Sky Survey. For the GLG and 36W sensitivity maps, the contour levels are 0.6, 0.65, 0.7, ..., 1.0, 1.25, 1.5, ..., 3.0 mJy beam $^{-1}$. The jagged edges of the GLG sensitivity map are due to the shapes of the facets discussed in § 2.2.1. For the 37W sensitivity map, the contour levels are 0.1, 0.15, 0.2, ..., 1.0 mJy beam $^{-1}$, and for the Braun sensitivity map, the contour levels are 0.025, 0.035, 0.045, 0.05, 0.06, ..., 0.1, 0.25 mJy beam $^{-1}$.

method, we generated maps with a typical noise level of ~ 0.6 mJy beam $^{-1}$ and a signal-to-noise ratio of ~ 1000 around the strongest sources—equivalent to that of the highest quality low-frequency radio images.

2.2.2. Generating the Source List

Sources in the first (Images A) and second (Images B) set of images were found using the MIRIAD task SFIND (ver. 2.0), which uses a false discovery rate (FDR) algorithm to detect sources (Hopkins et al. 2002). This algorithm is similar to a Gaussian source-finding algorithm, except that it also accounts for noise variations on a user-defined size (the *rmsbox* parameter). For each one of the central 73 facets, we made six

source lists. The first three source lists were made using *rmsbox* = 1.25, 1.88, and 2.5 beams (20, 30, and 40 pixels). Multiple values were used for the *rmsbox* parameter because sources the size of *rmsbox* were often missed by SFIND, and values of *rmsbox* larger than 2.5 beams caused SFIND to miss many sources. For the different values of *rmsbox*, SFIND detected a similar number of sources but there were sources found for one value but not others. These three source lists were then compiled into one list. Since the facets overlapped slightly, sources on the edge of a facet were “discovered” more than once. When merging the source list of each facet into a single source list, the source with the strongest signal-to-noise from this set of duplicates was kept. SFIND also had difficulty

TABLE 2
OBSERVATION PROPERTIES
A. OBSERVED SOURCES

Source	Integration Time (minutes)	Number of Visibilities
3C 405	25.8	47330
TXS 0035+413	23.1	42250
M31	239.5	438657

B. RECEIVER PROPERTIES		
IF Number	Frequency (MHz)	Bandwidth (Channel Separation) (kHz)
1.....	327.50	3125.0 (48.83)
2.....	321.56	3125.0 (48.83)

C. PRIMARY BEAM PROPERTIES	
Property	Value
Full width at half-maximum	138'
Field of view.....	7.6 deg ²
Resolution	6" × 6"
rms at center of field.....	0.61 mJy

D. GENERAL PROPERTIES	
Property	Value
Date of observation.....	2000 Dec 15
Pointing center (J2000).....	R.A. = 00 ^h 42 ^m 45 ^s .9, decl. = 41°16'18"0

with large and/or complicated sources, the integrated properties of these sources were determined by running SFIND without its FDR capabilities⁴ on maps smoothed to a resolution of $20'' \times 20''$. In these smoothed maps, a complicated source (e.g., a resolved radio jet) would be unresolved, allowing SFIND to better determine its integrated properties. As with the high-resolution maps, three source lists were made, each with a different value of *rmsbox*, *rmsbox* = 3.13, 6.25, and 9.38 beams (50, 100, and 150 pixels). Again, these three source lists were compiled into one. Once the final high-resolution and smoother source lists were made, they were compiled into one. In the case where a source in the smoothed map overlapped many sources in the high-resolution maps, the smoothed source was kept. Sources that appeared only in the smoothed maps were kept as well. However, in all other cases the source in the high-resolution maps were kept. The positions and sizes of sources found in Images A (Source list I) defined the clean boxes (CLEAN Boxes 2) used to make the second and final set of images (Images B). The final source list presented here (hereafter the GLG source list), given in Table 3, was made from Images B using this procedure. The location of these sources is shown in Figure 3.

2.3. Source Properties

The MIRIAD task SFIND determines the R.A., decl., local flux density rms σ_{rms} , peak brightness I , integrated flux density S , image major axis θ_M , image minor axis θ_m , and position angle θ_{PA} of every source it finds. Sources were separated into

four morphological categories—unresolved (U), elongated (El), complex (C), and extended (Ex)—defined in the following way:

1. Unresolved sources are sources in the high-resolution image with $\theta_M < 2 \times \theta_m$.
2. Elongated sources are also sources in the high-resolution image, but with $\theta_M \geq 2 \times \theta_m$. In practice, the major distinction between unresolved and elongated sources is that the major axis is resolved for elongated sources.
3. Complex sources are sources in the smoothed maps that overlap several sources in the high-resolution maps.
4. Extended sources are sources in the smoothed maps that do not overlap sources in the high-resolution maps. We defined “ExG” sources to be extended sources detected in other radio surveys of M31. Extended sources without counterparts in other radio surveys (“Ex” sources) are *most likely false detections* but are included here for completeness.

A total of 405 sources were detected: 281 are unresolved, 16 elongated, 51 complex, and 57 extended—of which two are ExG sources.

The source flux density S was calculated by correcting the value returned by SFIND for primary beam attenuation. After the primary beam correction was applied, the errors in θ_M , θ_m , and θ_{PA} of each source were calculated using equations (29a), (29b), and (30) in Condon et al. (1998). In this calculation, we assumed that the signal-to-noise of a source is equal to S/σ_{rms} . We also calculated the error in integrated flux density (S) and peak brightness (I) using equations (36a) and (37) in Condon et al. (1998) for a resolved (C, Ex, and ExG) source, equations (39) and (41) in Condon et al. (1998) for a source where only the major axis is resolved (El), and equation (43) in Condon et al. (1998) for an unresolved (U) source. However,

⁴ Without the FDR algorithm, SFIND works like other Gaussian source finding programs—looking for regions with a signal-to-noise ratio greater than a user-defined value. In our case, we instructed SFIND to keep all $\geq 5 \sigma$ sources.

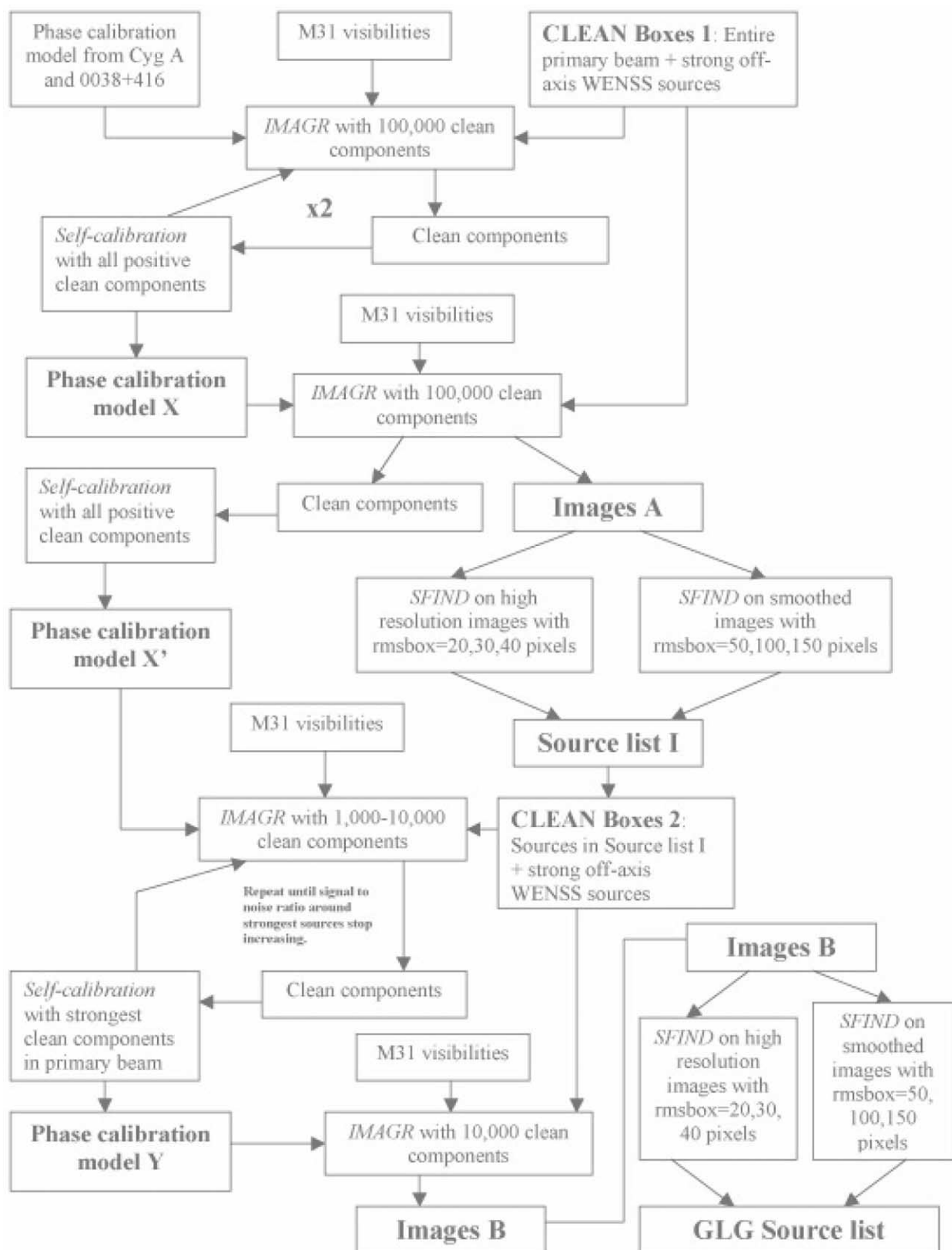


FIG. 2.—Flow chart of the data reduction described in §§ 2.2, 2.2.1, and 2.2.2.

TABLE 3
GLG SOURCE LIST

Name	Type	R.A. σ_α (arcsec)	Decl. σ_δ (arcsec)	θ_{M31} (arcmin) R_{M31} (kpc)	θ_M (arcsec) $\sigma(\theta_M)$	θ_m (arcsec) $\sigma(\theta_m)$	θ_{PA} (deg) σ_{PA}	I (mJy beam $^{-1}$) σ_A	S (mJy) σ_S	σ_{rms}	α φ
GLG 001	U	00 42 50.40 0.34	+41 16 10.28 0.40	0.8 0.7	5.7 0.4	4.6 0.3	15 6	7.94 0.70	8.26 0.70	0.69	-0.64 ± 0.06 ...
GLG 002	U	00 42 26.62 0.71	+41 18 04.62 0.66	4.0 3.9	4.9 1.4	4.5 1.2	76 155	4.17 0.59	3.65 0.59	0.63	-1.45 ± 0.34 0.13 ± 0.05
GLG 003	U	00 42 32.90 0.46	+41 11 43.57 0.48	5.1 1.4	5.0 0.6	4.7 0.5	14 26	5.12 0.53	4.76 0.53	0.54	-0.95 ± 0.02 ...
GLG 004	U	00 43 18.00 0.22	+41 17 21.94 0.19	6.1 4.2	10.0 0.1	7.7 0.0	67 6	7.37 0.70	22.85 0.70	0.60	-0.84 ± 0.14 0.04 ± 0.02
GLG 005	U	00 43 26.34 0.38	+41 19 12.04 0.41	8.1 4.5	5.7 0.4	5.3 0.4	12 14	6.60 0.62	7.97 0.62	0.67	≤ -1.15 ...

NOTES.—Units of right ascension are hours, minutes, and seconds, and units of declination are degrees, arcminutes, and arcseconds. Table 3 is available in its entirety in the electronic edition of the *Astrophysical Journal Supplement*. A portion is shown here for guidance regarding its form and content.

in all cases we set the “clean bias” term (σ_B in the NVSS paper; Condon et al. 1998) to 0 because restrictive clean boxes were used.

To check the flux calibration, we compared the flux densities of GLG sources with the flux densities of their counterparts in the WENSS catalog (Rengelink et al. 1997), which was also conducted at 325 MHz. Figure 4 compares the WENSS and GLG flux density for all GLG sources with a “good” match in the WENSS catalog, determined using the criteria discussed below in § 4.3. In general, there is good agreement between the flux densities measured by the WENSS and GLG surveys, particularly for the strongest sources and unresolved sources—implying that the flux calibration is correct.

After the flux errors were calculated, the positions of the GLG sources were registered to those of the strongest NVSS

sources. This was done by first finding all GLG sources that overlapped a NVSS source with $S_{1400} \geq 15$ mJy, because the positions of these NVSS sources is known to better than $1''$ and match those in the optical reference frame to ~ 40 mas (Condon et al. 1998). Figure 5 shows the offsets between the positions of these 15 GLG sources and their NVSS counterparts. The average R.A. offset between the GLG and NVSS sources was $-0''.099 \pm 0''.067$, and the average decl. offset was $0''.115 \pm 0''.067$, the error being the standard error in the mean. Every source in the GLG source list was then shifted by the average offset, and the intrinsic uncertainty in R.A. (ϵ_α) and decl. (ϵ_δ) were set to the error of the offsets. Errors in the positions of the GLG sources were then calculated with the formulae used for the NVSS source list (Condon et al. 1998).

3. SOURCE LIST

The final source list is presented in Table 3. The columns are as follows:

Column (1).—Name of the source. The sources are ordered in increasing distance from the center of the FOV.

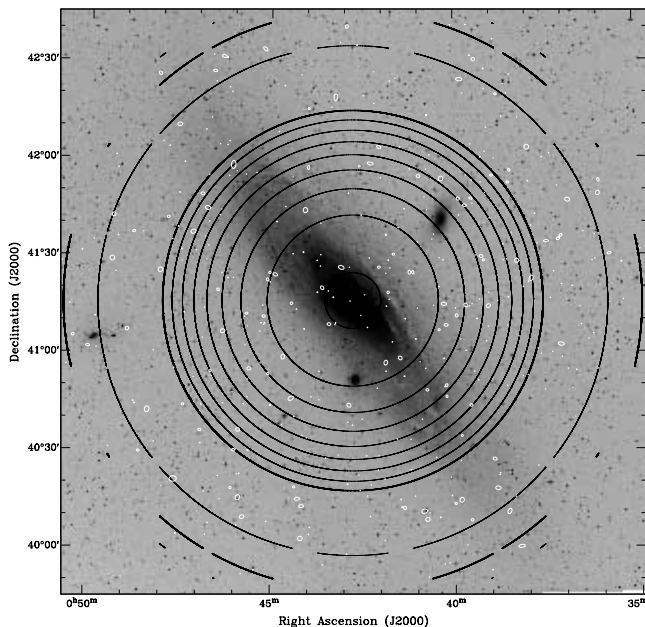


FIG. 3.—Palomar Optical Sky Survey image of M31 overlaid with the position of the GLG sources (white contours, representing the major and minor axis of the sources given in Table 3) and the 1σ sensitivity of the GLG survey (black contours). The sensitivity contours correspond to 0.6, 0.65, 0.7, 0.75, 0.8, 0.85, 0.9, 0.95, 1.0, 1.5, 2.0, and 2.5 mJy beam $^{-1}$.

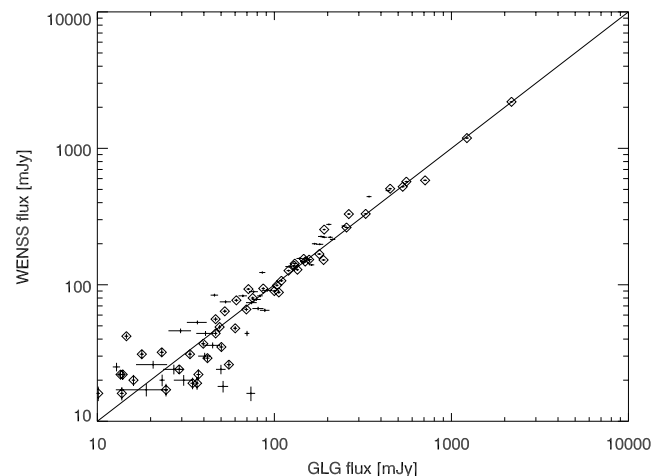


FIG. 4.—Flux density of WENSS sources with a “good” match (as defined in § 4.3) in the GLG catalog vs. flux density of corresponding GLG sources. The diamonds indicate an “U” or “EI” GLG source, and the sloping straight line indicates where the WENSS flux density equals the GLG flux density.

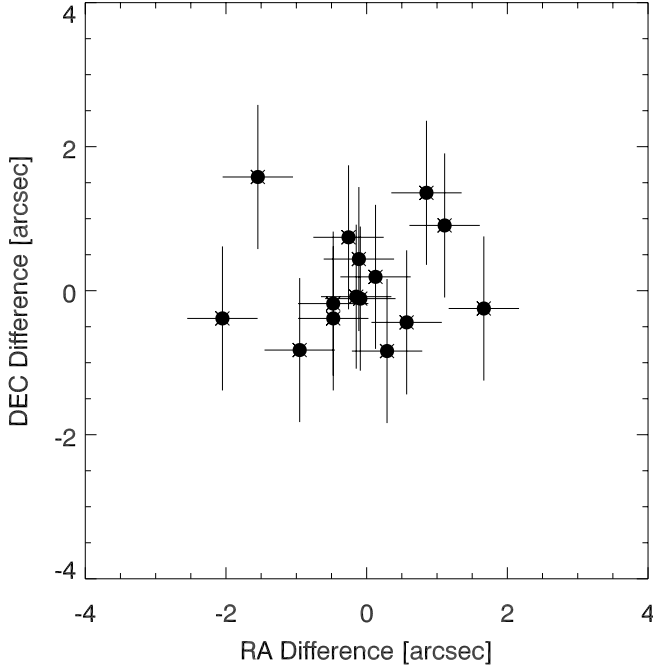


FIG. 5.—Positional offset (GLG-NVSS) between the 15 NVSS and GLG sources with $S_{1400} > 15$ mJy. These sources were used to register the location of the GLG sources.

Column (2).—Type of source. This is the morphological category of the sources as defined in § 2.3. The abbreviation “U” stands for unresolved, “El” for elongated, “C” for complex, “Ex” for extended, and “ExG” for an extended source with a counterpart in one or more other radio surveys of M31.

Column (3).—Right ascension of the source (J2000). Error in R.A. (σ_α) in arcseconds.

Column (4).—Declination of the source (J2000). Error in decl. (σ_δ) in arcseconds.

Column (5).— θ_{M31} , angular distance from the center of M31, in arcmin. R_{M31} , projected radius of source in M31 as defined in § 4.1, in kpc.

Column (6).—Major axis (θ_M) of the source, in arcseconds. Error in major axis [$\sigma(\theta_M)$] in arcseconds.

Column (7).—Minor axis (θ_m) of the source, in arcseconds. Error in minor axis [$\sigma(\theta_m)$] in arcseconds.

Column (8).—Position angle (θ_{PA}) north through east of the source, in degrees. Error in position angle (σ_{PA}) in degrees.

Column (9).—Peak brightness (I) of the source, in mJy beam $^{-1}$. Error in peak brightness (σ_I) in mJy beam $^{-1}$.

Column (10).—Integrated flux density (S) of the source in mJy. Error in integrated flux density (σ_S), in mJy.

Column (11).—Root mean square of the flux density around the source (σ_{rms}), in mJy.

Column (12).—Radio spectral index (α) of source, as calculated in § 4.3. Spectral curvature parameter (φ), as calculated in § 4.3. The spectral indices of Ex sources without a counterpart in another radio survey were not published because this source is most likely spurious, as mentioned in § 2.3. It is also possible that some of the steeper spectrum U sources ($\alpha < -2$) are spurious as well.

4. PROPERTIES OF OBSERVED SOURCES

We analyzed the statistical properties of this population to see if radio sources in the field of M31 field differed from

those elsewhere, and if so, how they differed. We analyzed both the radial, flux density, and spectral distribution of the GLG sources, and for comparison, data from the WENSS (Rengelink et al. 1997) and *XMM-Newton* Large-Scale Structure (*XMM-LSS*) radio survey (Cohen et al. 2003) surveys. The WENSS survey mapped the entire sky north of $\delta = 30^\circ$ at $\nu = 325$ MHz with a limiting flux density of 18 mJy and resolution of $54'' \times 82''$ around M31 (Rengelink et al. 1997), while the 325 MHz field of the *XMM-LSS* radio survey mapped a ~ 5.6 deg 2 region of sky with a resolution of $6''.3$ and a limiting flux density of 4 mJy beam $^{-1}$ —properties similar to the observation presented here (Cohen et al. 2003).

4.1. Radial Distribution of Observed Sources

If a substantial number of sources intrinsic to M31 were detected, we would expect to see an overdensity of sources in the optical disk of M31. In addition, any substructure present in M31 is most likely symmetric to some degree and might stand out in the radial distribution of sources. Unfortunately, interpreting the raw radial distribution of sources is difficult because the gain of the telescope decreases toward the edge of the FOV, as illustrated in Figure 1. As a result, faint sources detectable in the center of the FOV are undetectable at the edges, complicating models for the expected *observed* background radial distribution of sources. However, since the *XMM-LSS* 325 MHz observation was also done using one pointing of the VLA A configuration, its primary beam shape is very similar to that of this observation. Therefore, the effect of the primary beam’s shape on the radial distribution of sources should be the same for these two data sets. As a result, the *XMM-LSS* 325 MHz data provide a good background radial distribution for this comparison. The *XMM-LSS* radio survey also observed a “blank” field, so the radial distribution of the sources is dominated by instrumental effects and not by structure intrinsic to the program source.

We also compared the radial distribution of sources projected into the plane defined by the inclination of M31, which may contain more information about M31 itself. This was done by first converting the R.A. and decl. of each source in the GLG and *XMM-LSS* source list to angular coordinates (X , Y) relative to the center of M31 (or, for the *XMM-LSS* sources, the pointing center of that observation) using the IDL task WCSSPH2XY and then translating these angular coordinates into the plane of M31 on the sky (X_{M31} , Y_{M31}) using the following formulae:

$$X_{M31} = X \cos 52^\circ + Y \sin 52^\circ, \quad (1)$$

$$Y_{M31} = Y \cos 52^\circ - X \sin 52^\circ, \quad (2)$$

where 52° is the angle of the optical disk of M31 relative to north on the sky (Braun 1990). Since the plane of M31 is inclined 77° to the plane of the sky, a circle of radius R in M31 would be an ellipse in the (X_{M31} , Y_{M31}) coordinate system. Using this fact, the distance of a source from the center of the observation in the plane of M31 (R_{M31}) was calculated using the following formula:

$$R_{M31} = 780 \text{ kpc} \sqrt{X_{M31}^2 + \left(\frac{Y_{M31}}{\cos 77^\circ} \right)^2}. \quad (3)$$

As shown in Figure 6, there are substantial differences between the radial distribution of the *XMM-LSS* and GLG

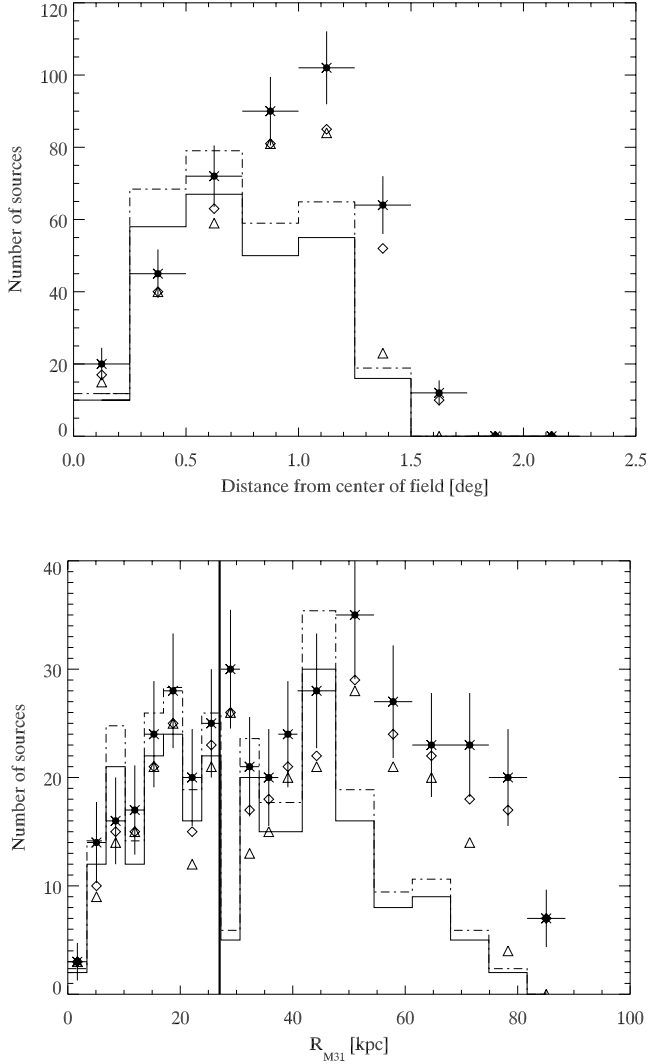


FIG. 6.—Radial distribution (*top*) and R_{M31} distribution (*bottom*; defined in § 4.1) of GLG (*filled circles*) and *XMM-LSS* survey (*solid line*) sources. The diamonds indicate all nonextended GLG sources, while the triangles are non-extended GLG sources with $S_{325} > 4$ mJy within $1^{\circ}34$ of the pointing center, i.e., the limits of the *XMM-LSS* survey (Cohen et al. 2003). The dot-dashed line is the distribution of the *XMM-LSS* survey scaled by the ratio of “triangle” GLG sources to *XMM-LSS* sources (see § 4.1 for details). The black vertical line in the bottom graph marks the outer edge of the optical disk of M31.

surveys. The first difference is the number of sources in the *XMM-LSS* (256) and GLG survey (405). Some of this difference is due to differences in the data analysis—the *XMM-LSS* list does not include sources found in smoothed maps (“Ex” GLG sources), only goes out to $1^{\circ}34$ from the pointing center (in the GLG survey, the furthest source is $1^{\circ}75$ from the pointing center), and does not include sources with $S_{325} < 4$ mJy (Cohen et al. 2003), while the GLG survey has a 5σ sensitivity of ~ 3 mJy. However, after applying the above limitations to the GLG source list there are still significantly (2.9σ) more GLG sources (302) than *XMM-LSS* sources (256).⁵ Some of this difference may be due to the fact that *XMM-LSS* source list was derived using the AIPS task VSAD (Cohen et al. 2003), a task similar to SFIND without its FDR capabilities, since the FDR algorithm allows SFIND to detect fainter sources than it would without it.

⁵ This implies a scaling factor of $302/256 = 1.18$ between the two surveys, used to generate the dot-dashed line in Fig. 6.

The second difference is in the distribution of sources between the GLG and *XMM-LSS* surveys—both in the plane of the sky and in R_{M31} . In the plane of the sky, the distribution of the *XMM-LSS* sources is relatively flat between $0^{\circ}25$ and $1^{\circ}25$, while the distribution of the GLG sources is rising in this range. This difference is even more pronounced in the R_{M31} distribution, where for $R_{M31} \gtrsim 50$ kpc, there are noticeably more GLG sources than *XMM-LSS* sources. Inside the optical disk of M31 ($R_{M31} \leq 27$ kpc), there are 145 GLG sources compared to 130 *XMM-LSS* sources, a $\sim 0.5\sigma$ excess. If one applies the criteria of the *XMM-LSS* survey to the GLG source list, there are in fact fewer (119) GLG sources than *XMM-LSS* sources. As a result, we expect that a majority of the GLG sources in the optical disk of M31 are background radio sources.

4.2. Flux Distribution

If the 325 MHz population of M31 had a characteristic flux density, then one would see an overdensity of GLG sources in a particular flux density range when compared with the flux distribution of the WENSS and *XMM-LSS* surveys. As with the radial distribution, the primary beam affects the measured flux distribution, but only at low flux densities. Therefore, we can compare the flux distribution of the GLG survey to that of both the WENSS and *XMM-LSS* surveys. Figure 7 shows that the flux distribution of GLG sources does not have an overdensity in a particular flux density bin or range of flux density bins—implying that the flux distribution of sources in M31 is not substantially different from that of background sources. However, given that we only expect to see a few sources in M31, they would need to be concentrated in one or two flux density bins for a difference to be detected.

In order to determine the completeness of the GLG survey, we compared the flux distribution with a model determined from the 327 MHz WSRT observations (Wieringa 1991). As shown in Figure 7, there is good agreement between the model and the observed flux distribution down to ~ 3 mJy—below the 5σ sensitivity of the observations (4 mJy; Wieringa 1991). Therefore, we estimate that the GLG survey is complete to between 3 and 4 mJy.

4.3. Spectral Properties

In general, the radio spectrum of a source can be expressed as a power law attenuated by some process. In this paper, we parameterize the attenuation as if it were the result of free-free absorption because this the major cause of low-frequency spectral turnover in Galactic objects. Therefore, we fit the observed spectrum to the following function:

$$S_{\nu} = S_{\nu_0} \left(\frac{\nu}{\nu_0} \right)^{\alpha} e^{-\varphi(\nu/1 \text{ GHz})^{-2.1}}, \quad (4)$$

where S_{ν} is the flux density of the source at a frequency ν , S_{ν_0} is the flux density of the source at frequency $\nu_0 = 324.5$ MHz, α is the radio spectral index, and φ is a parameter that measures spectral curvature. If the spectral curvature is truly the result of free-free absorption, then $\varphi > 0$ and corresponds to the optical depth owing to free-free absorption at $\nu = 1$ GHz, equal to (Condon 1992)

$$\varphi = 3.3 \times 10^{-7} (\text{EM}) \left(\frac{T_e}{10^4 \text{ K}} \right)^{-1.35}, \quad (5)$$

$$\text{EM} = \int n_e^2 dl, \quad (6)$$

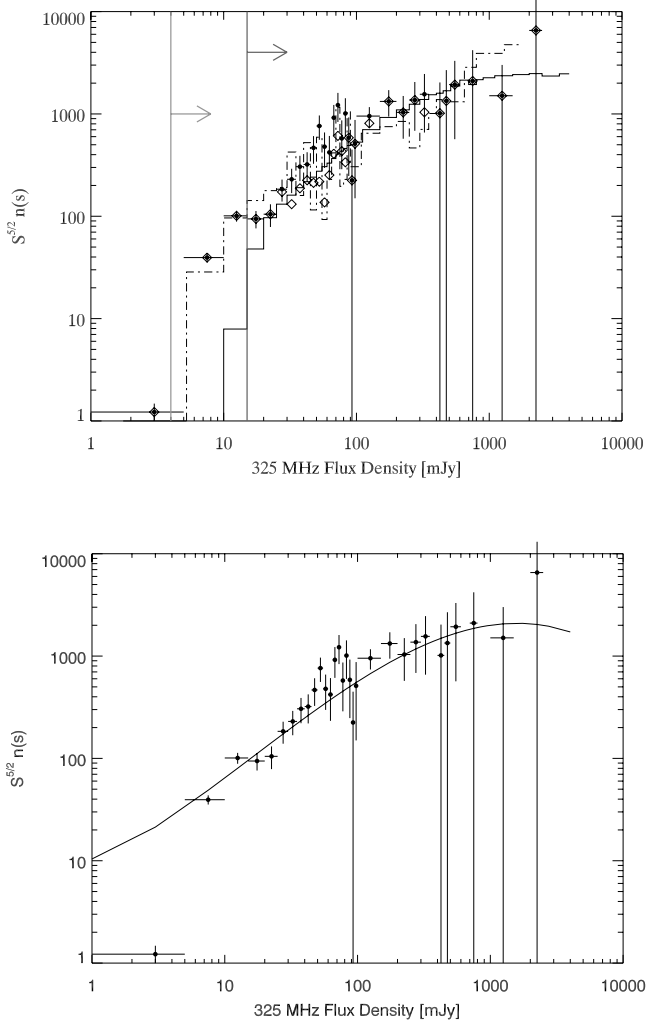


FIG. 7.—*Top*: The flux distribution of the GLG survey (*plus signs*), WENSS survey (*solid line*), and the XMM-LSS survey (*dot-dashed line*). The y -axis is $S_\nu^{5/2} n(S)$, where $n(S) = [N(S_0 < S < S_1)/(S_1 - S_0)]/\text{FOV}$ and $N(S_0 < S < S_1)$ is the total number of sources with flux density S between S_0 and S_1 . The $S_\nu^{5/2}$ term corrects for Euclidean geometry (Condon et al. 1998). The diamonds represent nonextended sources. The vertical lines represent the completeness limit of the XMM-LSS (*left*; Cohen et al. 2003) and WENSS (*right*; Rengelink et al. 1997) surveys. *Bottom*: The flux distribution of the GLG survey (*plus signs*) compared with the 327 MHz flux distribution model (*line*) derived from WSRT observations (Wieringa 1991).

where EM is the emission measure in units of $\text{cm}^{-6} \text{ pc}$, T_e is the electron temperature (in all EM calculations presented here we assume $T_e = 10^4 \text{ K}$), n_e is the electron density in units of cm^{-3} , and the integral in equation (6) extends over the line of sight to the object. For sources with an insufficient number of counterparts ($n_{\text{ctps}} \leq 3$) at other radio frequencies, the model used does not include the attenuation term and the spectrum was fit to a simple power law.

The surveys used to calculate the radio spectral index (α) and spectral turnover (φ) of the GLG sources were the 36W ($\nu = 610 \text{ MHz}$; Bystedt et al. 1984), 37W ($\nu = 1412 \text{ MHz}$; Walterbos et al. 1985), Braun ($\nu = 1465 \text{ MHz}$; Braun 1990), and NVSS ($\nu = 1400 \text{ MHz}$; Condon et al. 1998) surveys. The properties of these surveys are shown in Table 1. If a source in another catalog was less than

$$r = \text{Max} \left(\frac{\theta_M^{\text{GLG}} + \theta_m^{\text{GLG}}}{2}, \frac{\theta_M + \theta_m}{2} \right) \quad (7)$$

away from a GLG source, they were classified as a match, where θ_M^{GLG} is the major axis of the GLG source, θ_m^{GLG} is the minor axis of the GLG source (these are not the deconvolved values but the size of the source in our images), θ_M is the deconvolved major axis of the catalog source, and θ_m is the deconvolved minor axis of the catalog source (Braun 1990).⁶ A “good match” between a GLG source and a source in one of these catalogs was when the GLG had only one match in the other catalog and its counterpart only had no other matches in the GLG source list. The results of this comparison are summarized in Table 4. The number of false matches was calculated by shifting the position of the radio catalog in question by every combination of $\pm 1'$, $0'$ in R.A. and $\pm 1'$, $0'$ in decl. (except for a shift of $[0, 0]$), and calculating the number of matches and good matches in each combination. The number of false (good) counterparts reported in Table 4 is the average number of (good) matches detected in the eight shifted data sets, and the error in these values is the standard deviation of the number of (good) matches. As seen in Table 4, the number of false counterparts and false good counterparts are much less than observed. The WENSS survey has a larger number of false comparisons than the other surveys because its beam is much larger, resulting in a larger search radius. In order to avoid problems with source confusion, α and φ were calculated using only values from a “good match” by fitting the spectrum to the form defined in equation (4) using a least mean squares algorithm.

For GLG sources without a good counterpart in any of these radio surveys, we calculated the upper limit on the spectral index α . In order to do this, we made a sensitivity map⁷ of the 36W, 37W, and Braun surveys (shown in Fig. 1) by first making a sensitivity map of each pointing in the survey and then combining them together, weighing each pointing by $1/\sigma^2$, where σ is the rms of the pointing map. The upper limit was then determined by adjusting the stated minimum detectable flux density by the ratio of the survey’s sensitivity at the location of the source to the survey’s peak sensitivity. This was not necessary for the NVSS survey because our FOV is entirely within theirs, and an upper limit of $S_{1400} = 15 \text{ mJy}$ (the completeness limit of the NVSS survey) was used (Condon et al. 1998). The spectral index of these sources given in Table 3 is the flattest spectrum consistent with all nondetections. The spectral energy diagram (SEDs) of all GLG sources can be found in Figure 8, and the calculated α and φ of each source can be found in Table 3.

For sources with a “good match” in the 36W (610 MHz) survey and in at least one of the 1400 MHz surveys (NVSS, 37W, or Braun), it was possible to compare their α_{325}^{610} and α_{325}^{1400} spectral indices, the spectral index between 325 and 610 MHz and 325 and 1400 MHz, respectively. For sources with counterparts in multiple 1400 MHz radio catalogs, α_{325}^{1400} is the weighted average of the individual spectral indices. Figure 9 shows the graph of α_{325}^{1400} versus α_{325}^{610} for the 156 GLG sources that met this criteria. These sources are not evenly distributed around the $\alpha_{325}^{1400} = \alpha_{325}^{610}$ line; 99 GLG sources have $\alpha_{325}^{610} > \alpha_{325}^{1400}$, while only 57 have $\alpha_{325}^{610} \leq \alpha_{325}^{1400}$. A larger number of $\alpha_{325}^{610} > \alpha_{325}^{1400}$ sources is expected because the synthesized beam of the 36W survey is larger than that of any of

⁶ Because the 36W and 37W surveys were done with the Westerbork Radio Telescope (WSRT) as opposed to the VLA, there is a systematic offset in position between them and the GLG survey. However, this difference is $< 1''$, much smaller than the $> 6''$ radius used to search for counterparts.

⁷ A sensitivity map shows the rms of an observation over the field of view.

TABLE 4
COMPARISON WITH OTHER RADIO SURVEYS

Survey	Number of GLG Sources in Survey FOV	Number of GLG Sources with Counterparts	Number of GLG Sources with Good Counterparts	Number of False Counterparts	Number of False Good Counterparts	Reference
WENSS....	405	121	89	35.4 ± 8.2	16.3 ± 4.5	Rengelink et al. (1997)
36W.....	357	176	161	8.8 ± 2.1	4.3 ± 1.8	Bystedt et al. (1984)
37W.....	227	153	145	1.8 ± 1.6	1.4 ± 1.3	Walterbos et al. (1985)
Braun.....	87	67	53	9.8 ± 2.6	4.9 ± 2.4	Braun (1990)
NVSS.....	405	189	185	2.3 ± 1.6	2.1 ± 1.6	Condon et al. (1998)

the 1400 MHz surveys, meaning that the reported flux density of 36W sources possibly include emission resolved out in the 1400 MHz surveys. However, 23 of these sources have $|\alpha_{325}^{610} - \alpha_{325}^{1400}| > 3\text{Max}(\sigma_{\alpha_{325}^{610}}, \sigma_{\alpha_{325}^{1400}})$, where $\sigma_{\alpha_{325}^{610}}$ is the error of α_{325}^{610} and $\sigma_{\alpha_{325}^{1400}}$ is the error of α_{325}^{1400} , a statistically significant difference that cannot be explained by a difference in beam size. All but one of these sources have $\alpha_{325}^{610} > \alpha_{325}^{1400}$ —the signature of both free-free absorption and synchrotron self-absorption, and such sources have been observed in previous radio surveys, e.g., De Breuck et al. (2000). GLG 186, the only such source with $\alpha_{325}^{610} < \alpha_{325}^{1400}$ —has been categorized a variable source (see J. D. Gelfand, T. J. W. Lazio, & B. M. Gaensler 2004, in preparation, hereafter Paper II, for more information).

To determine if the GLG sources—both in and out of the optical disk of M31—had different spectral properties than background sources, we compared the S_{325} - α distribution (Zhang et al. 2003) and the α number distribution (Figs. 7 and 8 in De Breuck et al. 2000) of the GLG sources—shown in Figure 10—with that of sources in both the WENSS and NVSS survey. Both the S_{325} - α and α number distribution of GLG sources is consistent with the WENSS/NVSS results. We also compared the spectral index distribution of GLG sources with a higher frequency radio counterpart inside and outside the optical disk of M31 to see if there are any differences between these populations, also shown in Figure 10. While there are

substantial selection effects involved, e.g., the FOV of the deeper 1.4 GHz surveys are concentrated on the optical disk of M31 so steep sources outside M31 might be missed, there is no noticeable difference in the number distribution of α between these regions. However, this is not unexpected since the dominant radio sources of a galaxy—SNRs and H II regions—have similar spectral indices distributions than that of the dominant forms of background sources—FR I and FR II radio galaxies.

5. CONCLUSIONS

In this paper, we present the results of a high-resolution ($6''$) 325 MHz survey of a 7.6 deg^2 field centered on M31. In this data set, we identified 405 discrete sources (the “GLG” source list) and determined their size, orientation, and flux density. Through comparisons with 610 and 1400 MHz radio surveys of the same region, we calculated the spectral index α and spectral curvature φ of these sources.

To determine the nature of the GLG source list, we compared its properties to that of source lists derived from blank-field and/or large-area radio surveys—the WENSS, NVSS, and *XMM*-LSS radio surveys. A comparison of the radial distribution of GLG and *XMM*-LSS radio sources—both in the plane of the sky and in the plane of M31—showed that there is not a significant concentration of sources in the optical disk of M31. However, there does appear to be an excess of GLG sources at the edge of the field of view. The reason for this is unknown, but most likely caused by the different source

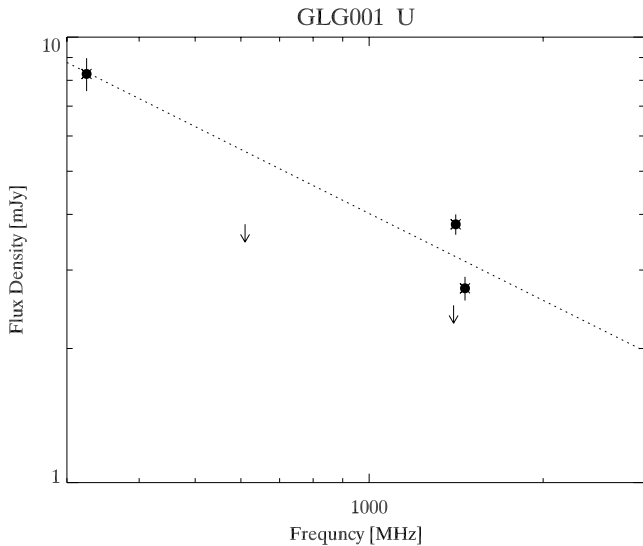


FIG. 8.—Radio spectrum ($\nu = 325$ –1400 MHz) of all GLG sources. A filled circle represents a good match, an arrow represents an upper limit, an open square on the x-axis represents a “bad match” (the GLG source either had more than one counterpart in this catalog or the catalog source had more than one counterpart in the GLG source list), and the dashed line is the best fit to eq. (4). The upper limits are scaled by the local rms of the survey in question. [See the electronic edition of the *Journal* for additional panels of this figure.]

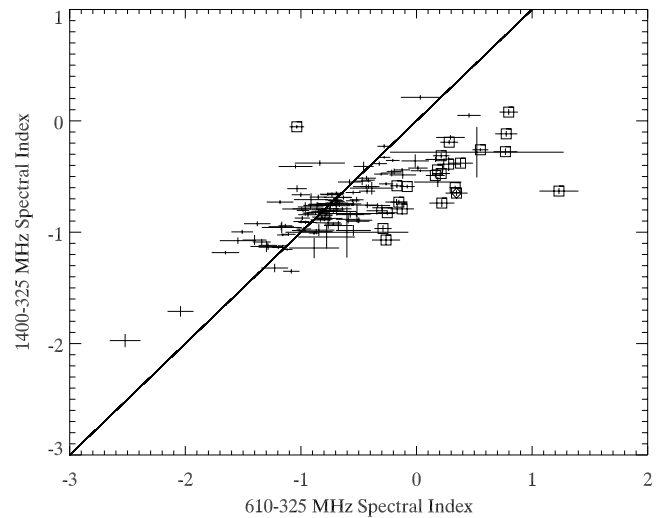


FIG. 9.—“Color-color” diagram of all 156 GLG sources with a good match in the 36W catalog and at least one of the 1400 MHz catalogs. The diamond is the one extended source that met this criteria, and the squares are sources with $|\alpha_{325}^{610} - \alpha_{325}^{1400}| > 3\text{Max}(\sigma_{\alpha_{325}^{610}}, \sigma_{\alpha_{325}^{1400}})$.

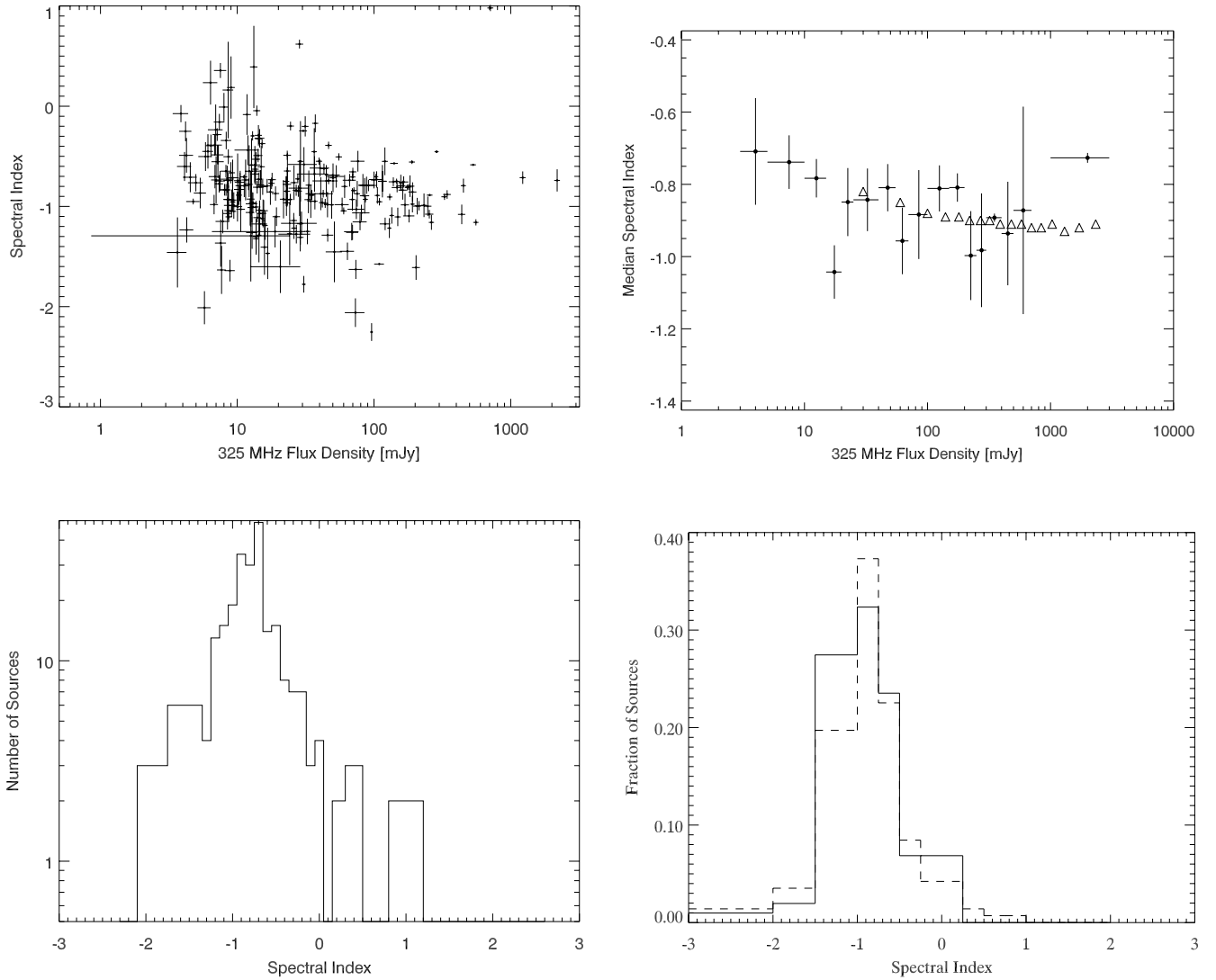


FIG. 10.—Clockwise from top left: α vs. S_{325} for the 244 GLG sources with a good counterpart in at least one other radio catalog; median spectral index vs. 325 MHz flux density for these sources (data points are a binned version of the top left graph, and the error bars are the standard deviation of spectral index in the S_{325} bin) overlaid with the results from the WENSS-NVSS surveys (triangles; Zhang et al. 2003); fraction distribution of α for sources inside (solid line) and outside (dashed line) the optical disk of M31; and number distribution of α .

finding programs used between the surveys. A comparison between the flux distribution of GLG sources with that of the WENSS and *XMM*-LSS radio surveys revealed no statistically significant overdensity or underdensities in a sizable flux range. The α number distribution of GLG sources was similar to that of sources in both the WENSS and NVSS radio surveys, as was the relationship between 325 MHz flux density S_{325} and α . The spectral index distribution of sources within the optical disk of M31 was also similar to that of sources in outside the optical disk of M31. All of this implies that the GLG source list is dominated by background radio galaxies and not sources intrinsic to M31.

In an accompanying paper (J. D. Gelfand, T. J. W. Lazio, & B. M. Gaensler 2004, in preparation), we compare the GLG source list with that of far-IR, IR, optical, and X-ray catalogs of this region and use this multiwavelength information, as well as the morphology and spectral index/curvature of a source, to determine the nature of individual sources. Through the method described in that paper, we have identified five supernova remnant and three pulsar wind nebulae candidates in M31, as well as a galaxy merger, BL Lac candidate, Giant

Radio Galaxy candidate, and several low-frequency variable and ultrasteepest spectrum ($\alpha < -1.6$) sources.

The authors thank Andrew Hopkins for providing us with the latest version of SFIND. T. J. W. L. acknowledges that basic research in radio astronomy at the NRL is supported by the Office of Naval Research. J. D. G. thanks Elias Brinks, Mike Garcia, Phil Kaaret, Albert Kong, Linda Schmidtobreck, Sergey Trudolyubov, Rene Walterbos, Ben Williams, C. Kevin Xu, and the SIMBAD help desk for providing us with source lists and/or images; Carole Jackson for providing her model of the flux distribution of background radio galaxies at 325 MHz; and Aaron Cohen, Elly Berkhuijsen, Jim Cordes, Rosanne DiStefano, Mike Garcia, Dan Harris, John Huchra, Namir Kassim, Albert Kong, Pat Slane, Krzysztof Stanek, Lorant Sjouwerman, Ben Williams, and Josh Winn for useful discussions; and the Harvard CDF for computer access.

The National Radio Astronomy Observatory is a facility of the National Science Foundation operated under cooperative agreement by Associated Universities, Inc. This research

has made use of NASA's Astrophysics Data System; of the SIMBAD database, operated at CDS, Strasbourg, France; of the NASA/IPAC Extragalactic Database (NED), which is operated by the Jet Propulsion Laboratory, California Institute of Technology, under contract with the National Aeronautics and Space Administration; of data products from the Two Micron All Sky Survey, which is a joint project of the University of

Massachusetts and the Infrared Processing and Analysis Center/California Institute of Technology, funded by the National Aeronautics and Space Administration and the National Science Foundation; and of the NASA/IPAC Infrared Science Archive, which is operated by the Jet Propulsion Laboratory, California Institute of Technology, under contract with the National Aeronautics and Space Administration.

REFERENCES

- Baars, J. W. M., Genzel, R., Pauliny-Toth, I. I. K., & Witzel, A. 1977, *A&A*, 61, 99
- Braun, R. 1990, *ApJS*, 72, 761
- Bystedt, J. E. V., Brinks, E., Schwering, P. B. W., Walterbos, R. A. M., de Bruyn, A. G., Israel, F. P., & Shane, W. W. 1984, *A&AS*, 56, 245
- Cohen, A. S., et al. 2003, *ApJ*, 591, 640
- Condon, J. J. 1992, *ARA&A*, 30, 575
- Condon, J. J., Cotton, W. D., Greisen, E. W., Yin, Q. F., Perley, R. A., Taylor, G. B., & Broderick, J. J. 1998, *AJ*, 115, 1693
- Cornwell, T. J., & Perley, R. A. 1992, *A&A*, 261, 353
- De Breuck, C., van Breugel, W., Röttgering, H. J. A., & Miley, G. 2000, *A&AS*, 143, 303
- Hopkins, A. M., Miller, C. J., Connolly, A. J., Genovese, C., Nichol, R. C., & Wasserman, L. 2002, *AJ*, 123, 1086
- Rengelink, R. B., Tang, Y., de Bruyn, A. G., Miley, G. K., Bremer, M. N., Roettgering, H. J. A., & Bremer, M. A. R. 1997, *A&AS*, 124, 259
- Stanek, K. Z., & Garnavich, P. M. 1998, *ApJ*, 503, L131
- Walterbos, R. A. M., Brinks, E., & Shane, W. W. 1985, *A&AS*, 61, 451
- Wieringa, M. H. 1991, Ph.D. thesis, Univ. Leiden
- Zhang, X., Reich, W., Reich, P., & Wielebinski, R. 2003, *A&A*, 404, 57